

## Article

# Effect of an Innovative Friction Damper on Seismic Responses of a Continuous Girder Bridge under Near-Fault Excitations

Junjun Guo <sup>1</sup>, Huaifeng Li <sup>2</sup>, Changyong Zhang <sup>2</sup>, Shihyu Chu <sup>3</sup> and Xinzhi Dang <sup>1,\*</sup>

<sup>1</sup> State Key Laboratory of Disaster Reduction in Civil Engineering, Tongji University, 1239, Siping Road, Shanghai 200092, China; guojj@tongji.edu.cn

<sup>2</sup> Shandong Provincial Communications Planning and Design Institute, Jinan 250031, China; bgs@sdcpd.com (H.L.); kjxx@sdcpd.com (C.Z.)

<sup>3</sup> Department of Civil Engineering, National ChengKung University, No. 1 University Road, Tainan 701, Taiwan; sychu@mail.ncku.edu.tw

\* Correspondence: 021tjdangxz@tongji.edu.cn

**Abstract:** Continuous girder bridges have been extensively constructed in China over the past 30 years, and these bridges tend to experience severe damage under ground motions with velocity pulses. In the current research, an innovative linear friction damper (LFD) is proposed to mitigate the seismic damages of continuous girder bridges subjected to near-fault ground motions. The OpenSees platform is adopted to establish the numerical model of a continuous girder bridge in the near-fault region. Sixteen ground motions with velocity pulses are selected from the PEER ground motion database. The wavelet method is used to extract the maximum velocity pulse from the two orthogonal components of a ground motion. The effects of the initial gap, the coefficient of friction, and the spring stiffness of LFD on the seismic responses of the bridge are investigated by the response surface method (RSM). The seismic responses of the bridge for the original system (Non-isolated), LFD system (Isolated-LFD), and lead rubber bearing (LRB) system (Isolated-LRB), such as force–displacement relationship, bearing displacement, and pier curvature, are obtained after conducting a series of nonlinear time history analyses. The numerical results reveal that this innovative device (LFD) can effectively control the relative displacements between the superstructure and substructure of the bridge. Meanwhile, the seismic responses of the piers can be significantly decreased compared with the non-isolated system.

**Keywords:** near-fault isolation; velocity pulses; continuous girder bridges; linear friction damper; lead rubber bearing



**Citation:** Guo, J.; Li, H.; Zhang, C.; Chu, S.; Dang, X. Effect of an Innovative Friction Damper on Seismic Responses of a Continuous Girder Bridge under Near-Fault Excitations. *Buildings* **2022**, *12*, 1019. <https://doi.org/10.3390/buildings12071019>

Academic Editors: Bo Wang and Rita Bento

Received: 7 June 2022

Accepted: 5 July 2022

Published: 15 July 2022

**Publisher's Note:** MDPI stays neutral with regard to jurisdictional claims in published maps and institutional affiliations.



**Copyright:** © 2022 by the authors. Licensee MDPI, Basel, Switzerland. This article is an open access article distributed under the terms and conditions of the Creative Commons Attribution (CC BY) license (<https://creativecommons.org/licenses/by/4.0/>).

## 1. Introduction

Continuous girder bridges have been widely constructed in China over the past 30 years. These bridges are characterized by expansion joints between adjacent segments to conform to displacement induced by temperature and fixed bearings at one of the piers to resist braking force. Unseating of the superstructure and pier collapse of girder bridges have been frequently observed in the past with strong earthquakes [1]. In the 2008 Wenchuan earthquake, the Huilan bridge was severely damaged, and it was found that the bearing on the top of the shortest pier was damaged first, and then, the pier with the largest flexural stiffness failed [2,3]. The girder may experience unseating at the expansion joint for a continuous girder bridge. Thus, it is essential to maintain the integrity of a continuous girder bridge. The inertial force of the superstructure should not be transmitted mainly through the pier with a fixed bearing.

Near-fault ground motions possessing strong velocity pulses impose high seismic demands for structures. The directivity effects occur when the fault ruptures toward the direction of the site at a speed approximately equal to the shear wave velocity [4]. Velocity pulses are characterized by a long period and short duration, leading to significantly larger

seismic responses than far-field ground motions [5]. For example, girder bridges will experience excessive relative displacement at expansion joints and severe damage at piers with fixed bearings. Passive control devices have been used to isolate the bridge deck from the substructure and to provide additional damping to dissipate input energy. These isolation systems, including bearings [6–11] and dampers [12–14], are widely adopted to control the seismic responses of bridges. However, these isolation devices might perform poorly under near-fault ground motions because large displacement caused by long-period velocity pulses can be difficult to accommodate by these systems [5]. Providakis [15,16] investigated the effect of supplemental damping on LRB seismic isolators under near-fault ground motions. The results revealed that the supplemental damping must be carefully controlled to avoid some adverse effects. Panchal and Jangid [17] studied the application of a variable friction pendulum system on structures under near-fault ground motions. It was found that this device can effectively control the seismic response of buildings subjected to near-fault ground motions. Dicleli et al. [18] conducted a parametric analysis to select the optimal isolator properties for bridges under near-fault ground motions. It was observed that energy dissipation devices are required to decrease the isolator displacements. Li et al. [19] found that shape memory alloy wire-based lead rubber bearings effectively control the deck displacement and reduce the internal forces of the pylon of cable-stayed bridges. Based on the research above, the isolation systems used to reduce the seismic responses of structures under near-fault ground motions should be characterized by large displacement capacity. Meanwhile, they should be able to control the relative displacement between the superstructure and substructure; thus, pounding and unseating can be avoided.

This paper aims to propose a linear friction damper (LFD) and validate the effectiveness of this device installed at continuous girder bridges in the near-fault region. First, this device's working mechanism, numerical validation, and design process are introduced in detail. Second, the numerical model of a continuous girder bridge is established using the OpenSees program. Third, 16 seismic records with strong velocity pulses are selected from the PEER website as input ground motions. Then, a parametric analysis of LFD is conducted to determine the appropriate parametric values for this device. Finally, the seismic responses of the bridge with the original system (Non-isolated), lead rubber bearing system (Isolated-LRB), and LFD system (Isolated-LFD), such as bearing displacement and pier curvature, are obtained after performing a series of nonlinear time history analyses. Comparisons are made between the original system and the isolation systems to evaluate the effectiveness of LFD in mitigating the overall seismic responses of bridges subjected to ground motions with velocity pulses.

## 2. Linear Friction Damper (LFD)

### 2.1. Working Mechanism of LFD

Figure 1 depicts a self-centering linear friction damper (LFD) composed of a guiding system and sliding block. The sliding block is rigidly connected with the superstructure and can move along the axial direction of the guiding rod. The guiding system comprises a slot, guiding rods, hinge plates, baffles, friction blocks, and springs. The bottom of the slot is fixed on the substructure, and both ends of the guiding rod are rigidly connected to the slot. The springs providing restoring force are rigidly connected with the slot and baffles. The hinge rods hinge plates, and the friction blocks are hinged. Thus, relative displacement will take place when they are subjected to force action. The working mechanism of LFD can be summarized as below: After the initial gap between the sliding block and slot is filled, the sliding block starts to push the hinge plate, and the friction blocks are forced to move outside. This movement is strongly restricted by the side plate of the slot. Thus, normal pressure between the friction block and slot takes place. Moreover, this force linearly increases with the movement of the sliding block. Meanwhile, the corresponding spring is also compressed to resist the force transmitted from the sliding block. In the unloading process, the direction of normal pressure will change to the opposite direction. The force–displacement relationship of LFD is illustrated in Figure 2. In the current study,

the angle between the hinge plate and the hinge rod is assumed to be 135 degrees. In the loading process (Figure 2a), the external force is resisted by the spring force and the friction force in the direction of displacement. In the preliminary research of the device, for brevity, it is assumed that the friction coefficient complies with the Coulomb friction law. Thus, the force–displacement relationship of LFD in the loading process can be obtained as below:

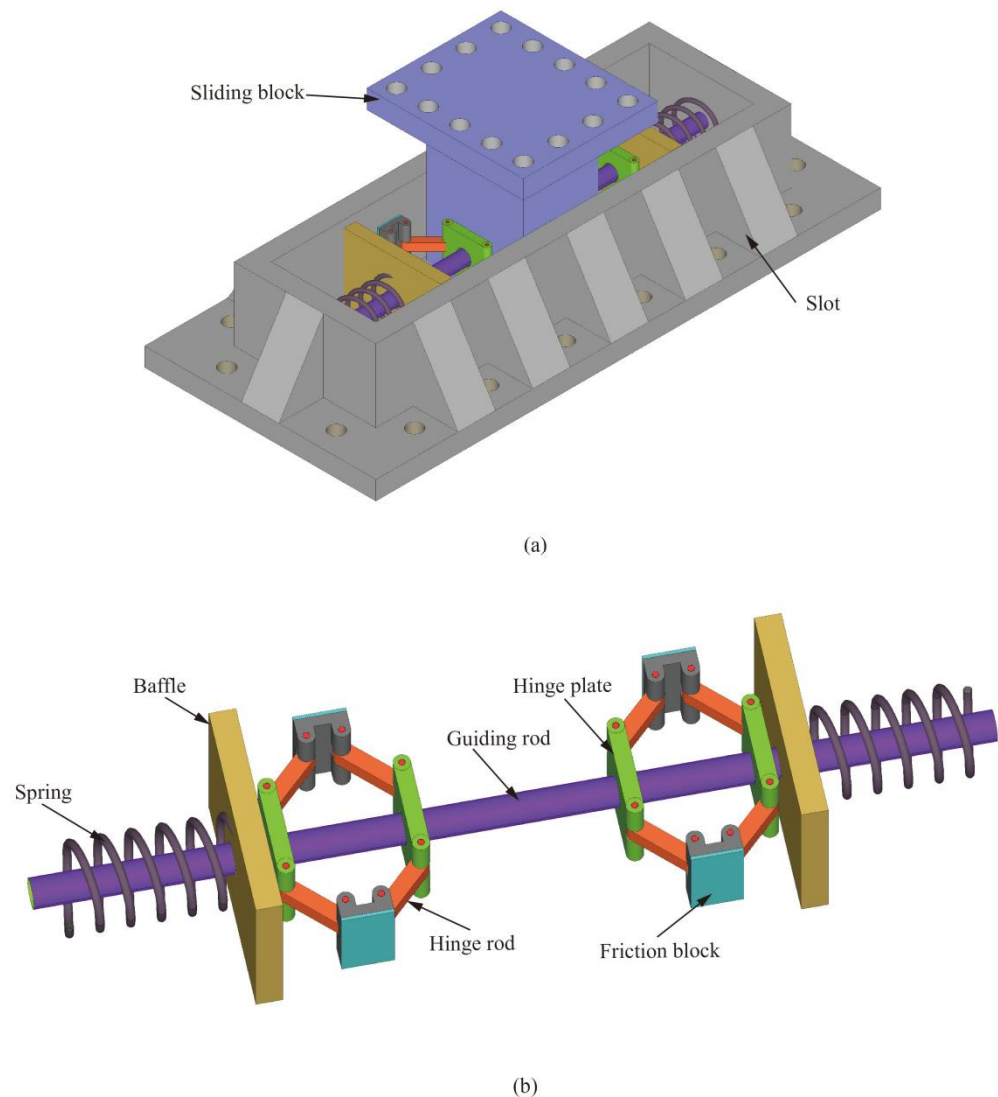


**Figure 1.** Schematic illustration of the linear friction damper (LFD): (a) general view of LFD; (b) internal details of LFD.

$$F = kd + 2f \quad (1)$$

$$f = \frac{kd + F}{2} \mu \quad (2)$$

$$F = \frac{1 + \mu}{1 - \mu} kd \quad (3)$$

where  $\mu$  is the friction coefficient,  $k$  is the spring stiffness, and  $d$  is the displacement. It can be found that the stiffness of LFD in the loading process is  $k(1 + \mu)/(1 - \mu)$ , which is larger than that of spring due to the contribution of the friction effect. In the unloading process (Figure 2b), the direction of the friction force  $f$  is reversed, and the spring force  $kd$

is balanced by the external force  $F$  and friction force  $f$ . As a result, the force–displacement relationship of LFD in the unloading process can be derived as below:

$$F = \frac{1 - \mu}{1 + \mu} kd \quad (4)$$

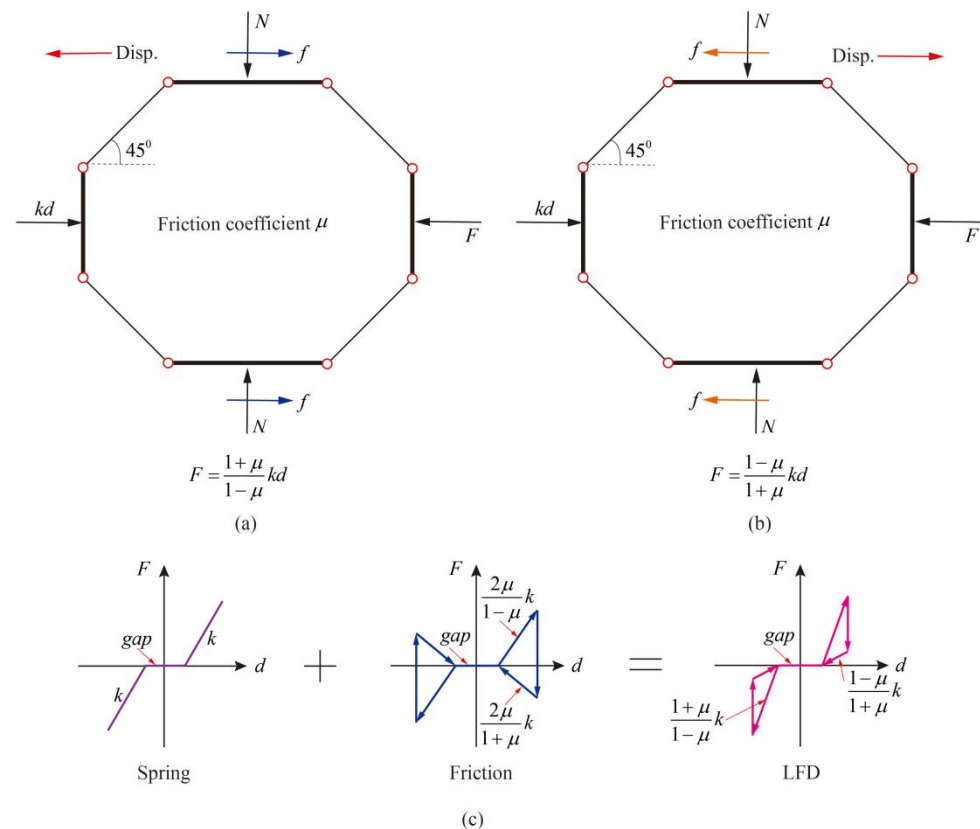


**Figure 2.** The working process of the LFD: (a) loading process; (b) unloading process; (c) constitutive model.

Based on the aforementioned analysis, the force–displacement relationship of LFD comprises two parts: spring and linear friction (Figure 2c). It is found that an initial gap can be set in LFD, and the device does not play its role until the initial gap is exhausted. The spring system can provide strong restoring force. Therefore, LFD can accommodate large displacements caused by velocity pulses and can effectively control the corresponding displacements.

## 2.2. Numerical Validation of LFD

A numerical experiment was conducted to validate the theoretical force–displacement relationship of LFD. Important features of the FE model are shown in Figure 3a. Only half of the model is considered for the numerical experiment. The slot, hinge rods, and friction blocks are modeled using linear eight-node solid elements. For brevity, the hinge parts are not precisely modeled, and constraint is adopted to simulate the hinge behavior. In addition, the spring in LFD is simulated by a linear elastic material with a stiffness of 2500 N/mm. The contact and friction behaviors between the slot and friction block are elaborately simulated. The Coulomb law is adopted to simulate the contact property of the surfaces in the tangential direction, and the friction coefficient is set to 0.2. Based on the previous research [20], the friction coefficient depends on contact pressure, sliding velocity, and air temperature. In the preliminary research of this new device, for brevity, the Coulomb friction law is used. The displacements of 50, 100, and 150 mm are applied to the loading point to obtain the force–displacement relationship of the device. Figure 3b

illustrates the Mises stress of the device in the loading process. Figure 4 compares the theoretical constitutive model and that of the numerical experiment. It is found that the theoretical model is consistent with that of the numerical experiment. Moreover, this theoretical constitutive model will be adopted in the following sections.

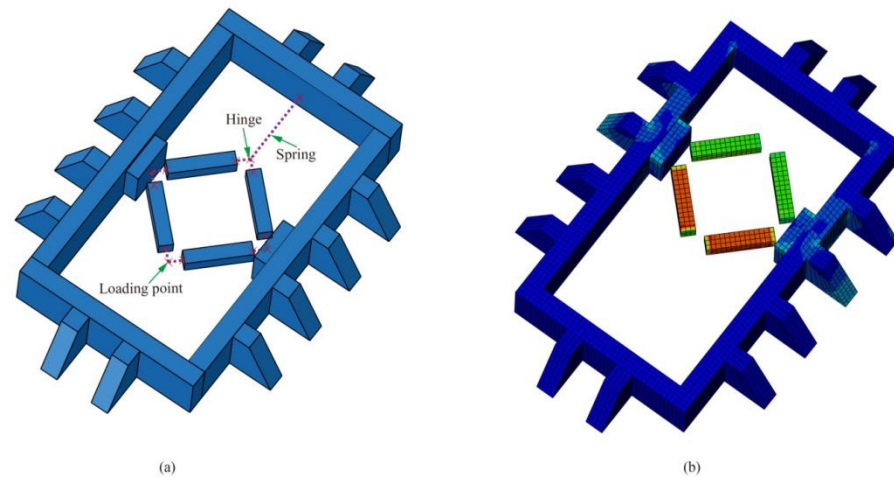


**Figure 3.** The numerical experiment of LFD: (a) arrangement; (b) Mises stress in the loading process.

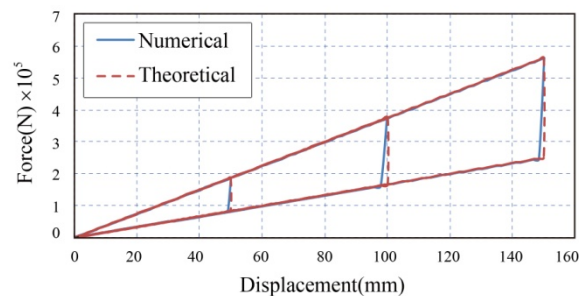


**Figure 4.** The theoretical constitutive model compared to that of the numerical experiment of LFD.

### 2.3. Design Process of LFD

LFDs can be installed either in the longitudinal or transverse direction of bridges, such as girder and cable-stayed bridges. The design flow chart of LFD is demonstrated in Figure 5. According to the force–displacement relationship, it is found that the critical parameters of LFD are the initial gap  $d_0$ , friction coefficient  $\mu$ , and spring stiffness  $k$ . The effects of spring stiffness on the seismic responses will be discussed in the following section in detail. For a specific case, first, the initial parametric values of LFD are assumed (for example, the friction coefficient can be determined by the material property of the contact surface, the initial gap can be set based on the displacement induced by temperature, and the initial stiffness can be set to 10,000 kN/m). LFDs and bidirectional sliding bearings replace the original bearing arrangement of the bridge. Second, a nonlinear time history analysis is performed to obtain the seismic responses of the critical components, such as superstructure displacement and pier curvature. Then, whether the seismic responses exceed their corresponding limits is examined. If the seismic responses are over their limit values, the parametric values of LFD should be reassumed. Otherwise, the current parametric values will be selected. Finally, the dimensional details of LFD are determined based on the parametric values and seismic responses of LFD.

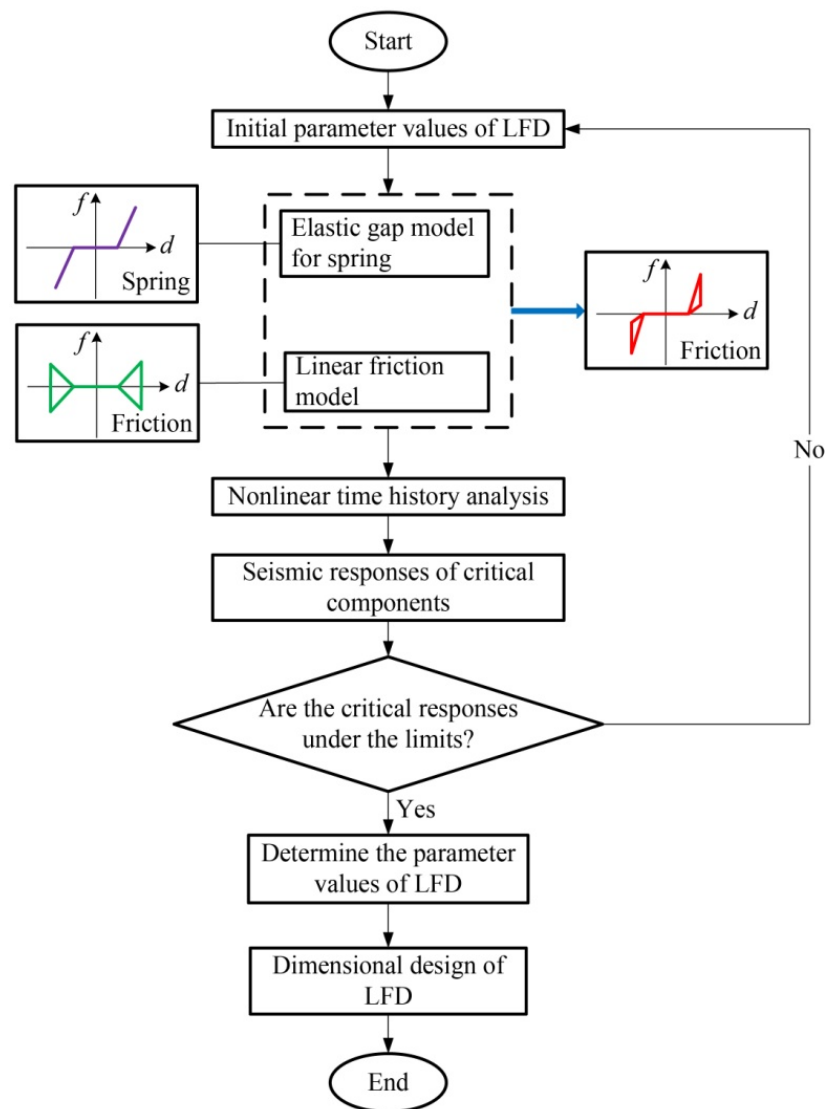
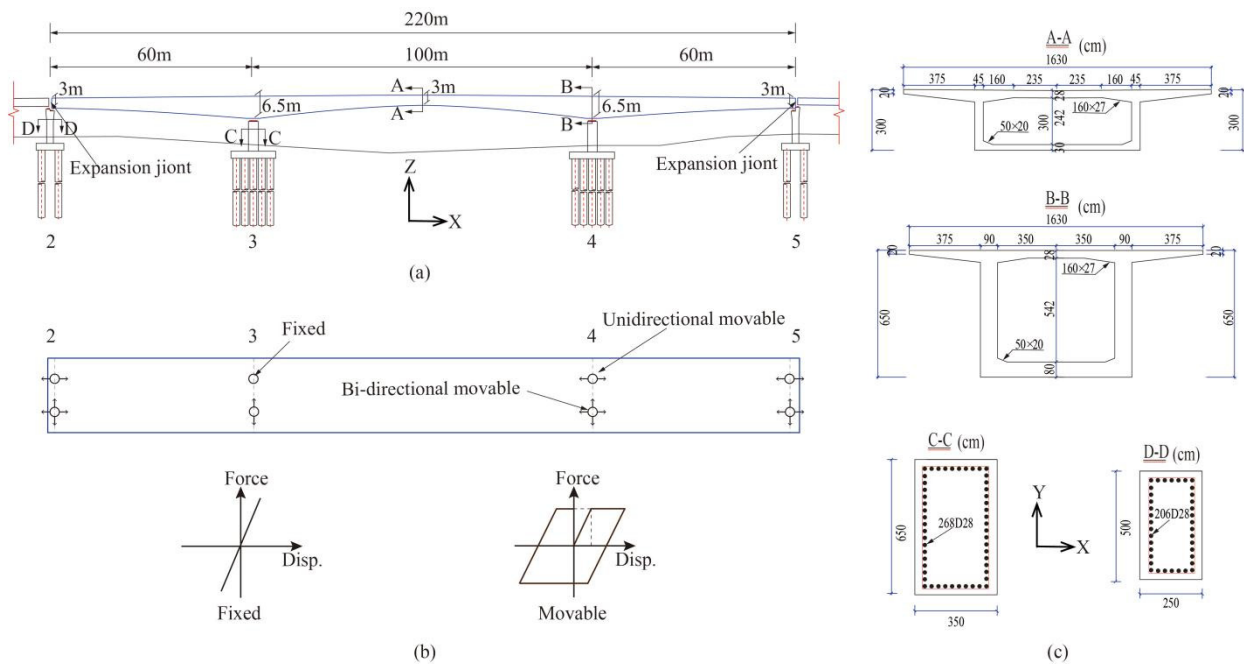


Figure 5. Design flow chart of the bridge installed with the LFD.

### 3. Continuous Girder Bridge

#### 3.1. Geometry Description

In order to evaluate the isolation effect of continuous girder bridges equipped with LFDs when subjected to near-fault ground motions, the current study adopts a three-span continuous box-girder bridge with typical configurations of girder bridges in China. Figure 6a illustrates the bridge's elevation with a main and side span length of 100 and 60 m, respectively. The concrete strength of the bridge is 29.2 MPa, and the yield strength of the reinforcement is 345 MPa. The height of the bridge girder varies from 3 to 6.5 m, and expansion joints are installed to accommodate displacement induced by temperature. The original bearing arrangement (Non-isolated) is presented in Figure 6b, including fixed bearing, unidirectional and bidirectional sliding bearings. As a result, the superstructure can freely deform in the longitudinal and transverse directions. Lead rubber bearings (LRBs), due to their high damping properties, are used worldwide [21]. Therefore, in the current study, the comparisons are made between the LRBs system (Isolated-LRB) and the LFDs system (Isolated-LFD) to evaluate the effectiveness of LFDs in mitigating the seismic responses of the bridge under near-fault ground motions. Figure 6c demonstrates the cross-sections of the box-girder and piers.



**Figure 6.** Description of the girder bridge: (a) elevation and (b) plan of the prototype bridge and (c) section properties.

### 3.2. Numerical Modeling

The OpenSees (the Open System for Earthquake Engineering Simulation) [22] platform is adopted to establish the numerical model of the bridge, as can be seen in Figure 7. In the current study, the superstructure is modeled as a spine, and the elastic beam–column element is used to simulate it because the deck is expected to maintain elasticity during seismic excitation. In order to account for pier nonlinearity, fiber sections composed of confined concrete, unconfined concrete, and longitudinal reinforcement are employed to establish piers. The model of Mander et al. [23] is adopted to simulate the confined concrete. Lumped linear springs, including three translational and rotational springs, model the pile foundations. In addition, the pile caps mass is lumped at their centers. Pot rubber bearings are used for the original bearing system (Non-isolated), and the bearing arrangement can be seen in Figure 6b. For the lead rubber bearing system (Isolated-LRB), the bearings in piers 3 and 4 are replaced with LRBs, as shown in Figure 7. Based on the vertical load capacity of LRB, the elastic stiffness ( $K_1$ ), post-yield stiffness ( $K_2$ ), and characteristic strength ( $Q_d$ ) of LRBs are set to 30,000 kN/m, 4500 kN/m, and 771 kN, respectively. For the linear friction damper system (Isolated-LFD), the bearings in pier 3 and 4 are replaced with bidirectional movable bearings and LFDs, as seen in Figure 7. In the current research, the ground motions excite the bridge only in the longitudinal direction, and the other two directions are not considered.

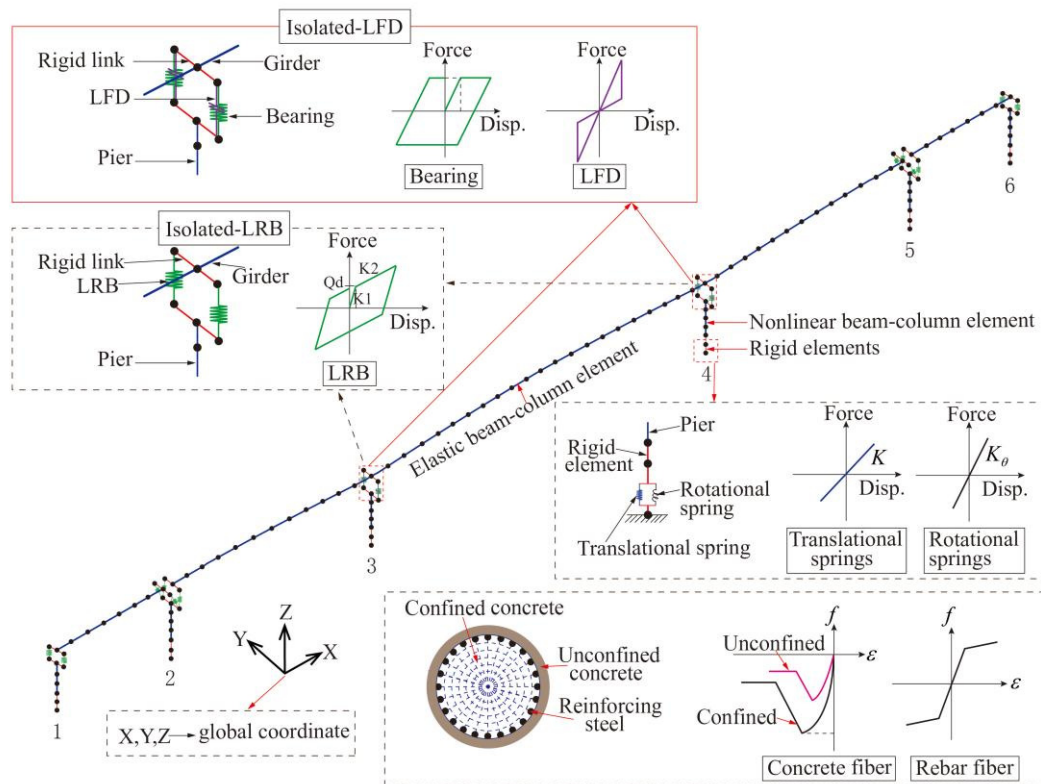


Figure 7. Numerical model of the prototype bridge.

#### 4. Near-Fault Ground Motions

To evaluate the directivity effects on the seismic responses of the prototype bridge, sixteen ground motions with velocity pulses were selected from the Pacific Earthquake Engineering Research Center database in the current study, as seen in Table 1. The magnitudes and pulse periods in Table 1 are varied from 5.8 to 7.62 and from 0.57 to 9.33 s, respectively. The original ground motion refers to a linear combination of two orthogonal components of a ground motion in the strongest velocity pulse direction. In the present study, the procedure developed by Baker [24,25] was adopted to extract the largest velocity pulse from an original ground motion. This procedure mainly contains two steps: First, Daubechies wavelet of order four is adopted to calculate the wavelet transform coefficients of the two orthogonal components of a ground motion, and the sum of the squares of these two coefficients sequences is compared to determine the largest velocity pulse direction. A linear combination of the two orthogonal components in the largest velocity pulse direction yields the original ground motion. Second, wavelet analysis is performed for the original ground motion to extract the largest velocity pulse, and the details are referred to in [24]. The peak ground accelerations (PGA), peak ground velocities (PGV), and pulse periods ( $T_p$ ) in Table 1 correspond to their original ground motions, as discussed previously. Figure 8 presents the largest velocity pulses extracted from the ground motions in Table 1, and these pulses are characterized by different shapes, peak ground velocities, and pulse periods. Thus, Daubechies wavelet of order four can effectively extract velocity pulses from ground motions. Figure 9 illustrates the velocity spectra of the original ground motion, extracted pulse, and residual ground motion for ground motions in Table 1. It can be found that velocity pulses possess long periods. In addition, the pulse periods are not always consistent with the maximum spectral periods of the original ground motions. For instance, the pulse period of the 13th ground motion in Table 1 is larger than its corresponding maximum spectral period of original ground motion. Therefore, it is more reasonable to determine pulse period from the aspect of time–frequency than from the view of frequency. In the

current research, the original ground motions in Table 1 are applied to the longitudinal direction of the prototype in the following sections.

**Table 1.** Ground motions with forward-directivity effects.

No.	Record Number	Earthquake Name	Year	Magnitude	Rrup (km)	PGA (g)	PGV (cm/s)	Tp (s)
1	4126	Parkfield-02_CA	2004	6	3.79	0.85	43.2	0.57
2	1052	Northridge-01	1994	6.69	7.26	0.53	56.1	0.73
3	568	San Salvador	1986	5.8	6.3	0.70	68.3	0.81
4	1004	Northridge-01	1994	6.69	8.44	0.75	77.8	0.92
5	1106	Kobe_Japan	1995	6.9	0.96	0.86	105.1	1.09
6	77	San Fernando	1971	6.61	1.81	1.38	121.7	1.64
7	723	Superstition Hills-02	1987	6.54	0.95	0.46	143.8	2.39
8	828	Cape Mendocino	1992	7.01	8.18	0.71	96.6	3.00
9	982	Northridge-01	1994	6.69	5.43	0.38	101.5	3.14
10	1085	Northridge-01	1994	6.69	5.19	0.84	113.9	3.61
11	1176	Kocaeli_Turkey	1999	7.51	4.83	0.28	90.6	4.95
12	1244	Chi-Chi_Taiwan	1999	7.62	9.94	0.39	108.8	5.34
13	1501	Chi-Chi_Taiwan	1999	7.62	9.78	0.18	78.9	6.55
14	879	Landers	1992	7.28	2.19	0.72	132.1	5.12
15	1502	Chi-Chi_Taiwan	1999	7.62	16.59	0.13	52.3	8.46
16	1482	Chi-Chi_Taiwan	1999	7.62	19.89	0.20	57.9	9.33

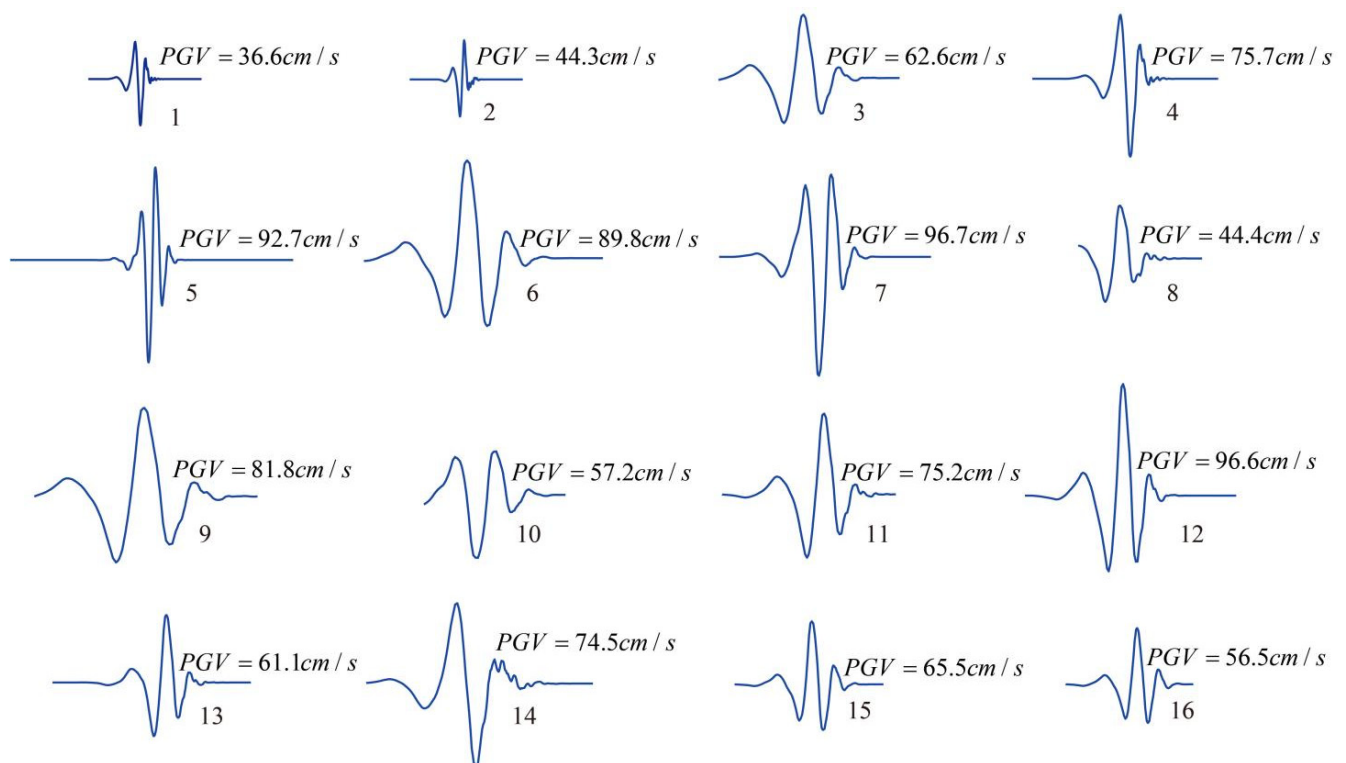


**Figure 8.** The strongest velocity pulses extracted from ground motions in Table 1.

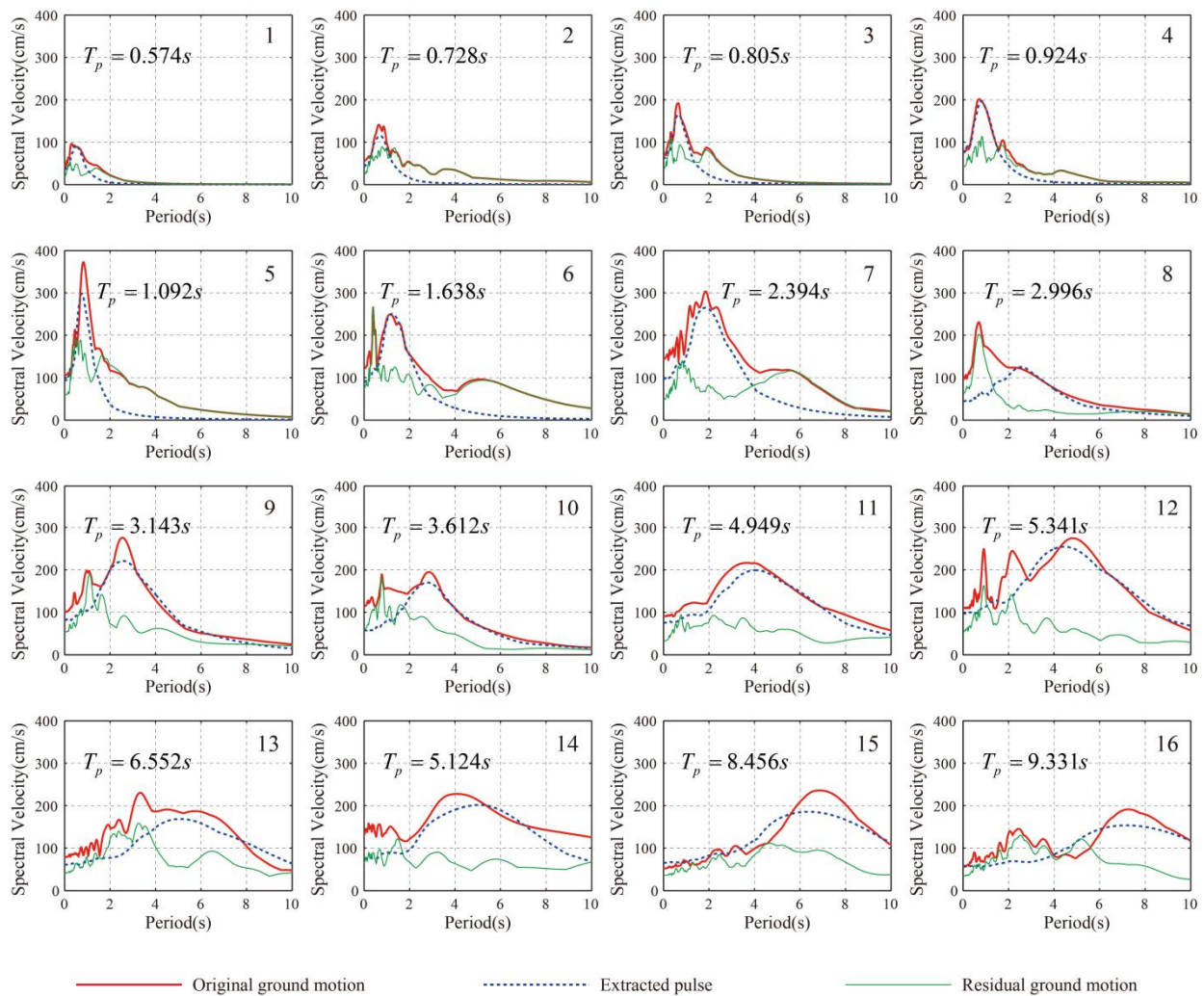


**Figure 9.** Velocity spectra of the original ground motion, extracted pulse, and residual ground motion for ground motions in Table 1.

## 5. Numerical Results and Discussion

### 5.1. Parametric Analysis of LFD

In this section, the Response Surface Method (RSM) [26] is used to obtain the optimal parametric values of LFD. The fundamental idea of RSM is to adopt a polynomial with multiple variables to simulate the real response surface [27]. More detailed information on RSM can be referred to in the work of Towashiraporn [28].

In the current study, the initial gap ( $x_1$ ), the coefficient of friction ( $x_2$ ), and the spring stiffness ( $x_3$ ) of LFD are regarded as design parameters. For each ground motion, 15 experimental design points are generated based on RSM, and nonlinear time histories are conducted to obtain the maximum pier curvatures and bearing displacements of the bridge at the design points. Figure 10 illustrates the contour maps of the maximum pier curvatures and bearing displacements with respect to the initial gap ( $x_1$ ), the coefficient of friction ( $x_2$ ), and the spring stiffness ( $x_3$ ) of LFD ground motions 1 and 7 in Table 1. It is found that the maximum pier curvatures increase with the increase in spring stiffness. Moreover, the initial gap ( $x_1$ ) significantly influences the bearing displacement. It also indicates that the coefficient of friction ( $x_2$ ) has little effect on the seismic responses of the bridge compared to the other two parameters. The large displacement accommodation should be considered for ground motions with velocity pulses.

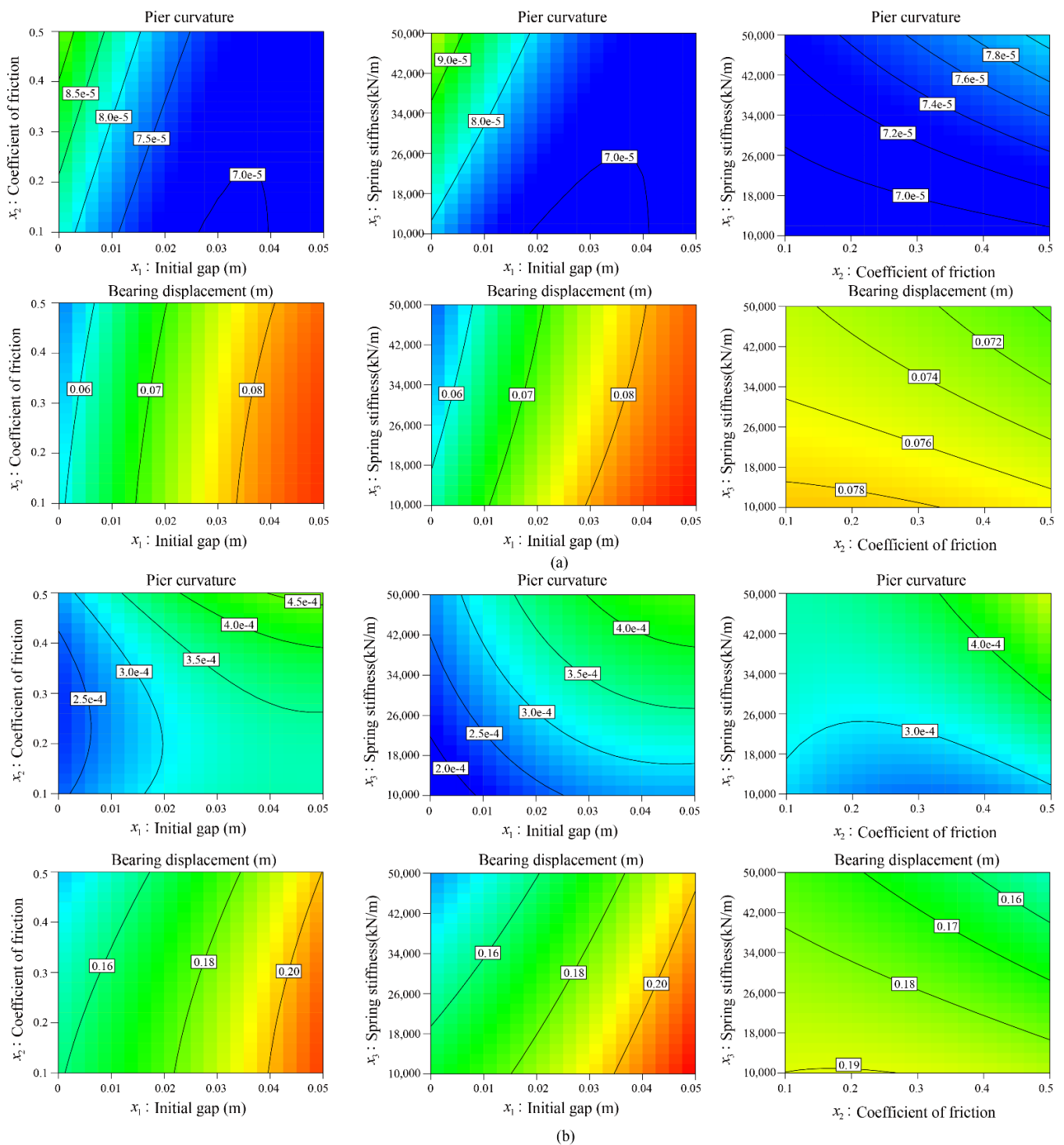


**Figure 10.** Contour maps of maximum pier curvature and bearing displacement with respect to the variables of initial gap ( $x_{21}$ ), coefficient of friction ( $x_2$ ), and spring stiffness ( $x_3$ ) of LFD: (a) wave 1 and (b) wave 7 in Table 1.

Furthermore, the maximum displacement between the superstructure and the substructure of the bridge should be limited to avoid pounding and unseating of the girders. However, this benefit is at the expense of increasing the pier damage. Therefore, proper device parameters should control the maximum relative displacement between the superstructure and the substructure to a reasonable range and should not significantly increase the seismic demand of the pier. Based on the above discussions, the spring stiffness of LFD

is set to 30,000 kN/m. In addition, the friction coefficient and initial gap of LFD are set to 0.2 and 0, respectively.

### 5.2. Force–Displacement Relationship of Components in the Longitudinal Direction

Figure 11 illustrates the force–displacement relationships of the bearing and pier of the prototype bridge with the original system (Non-isolated), LFD system (Isolated-LFD), and LRB system (Isolated-LRB) for waves 4, 9, and 14 in Table 1. For the original system (Non-isolated), the elastic perfectly plastic material is adopted to simulate the force–displacement relationship of the sliding bearing. The bearing starts to move when its friction force reaches a critical value. Meanwhile, for the LFD system (Isolated-LFD), the bearing system’s constitutive model comprises two parts: sliding bearing and LFD. In addition, for the LRB system (Isolated-LRB), the bearing yields when the shear force reaches the characteristic strength ( $Q_d$ ) of the bearing. It can be found that the LRB system (Isolated-LRB) usually experiences a larger bearing displacement than the other two systems. This phenomenon can explain that for the LRB system (Isolated-LRB), the second stiffness ( $K_2$ ) of the LRB bearing is much smaller than its initial stiffness. When a ground motion with a strong velocity pulse excites the bridge in the longitudinal direction, the small post-yielding stiffness of the LRB bearing cannot control the relative displacement induced by a large velocity pulse. Meanwhile, the LFD system (Isolated-LFD) can provide large constant stiffness in the loading process. Thus, the relative displacement between the superstructure and the substructure of the bridge can be effectively controlled.

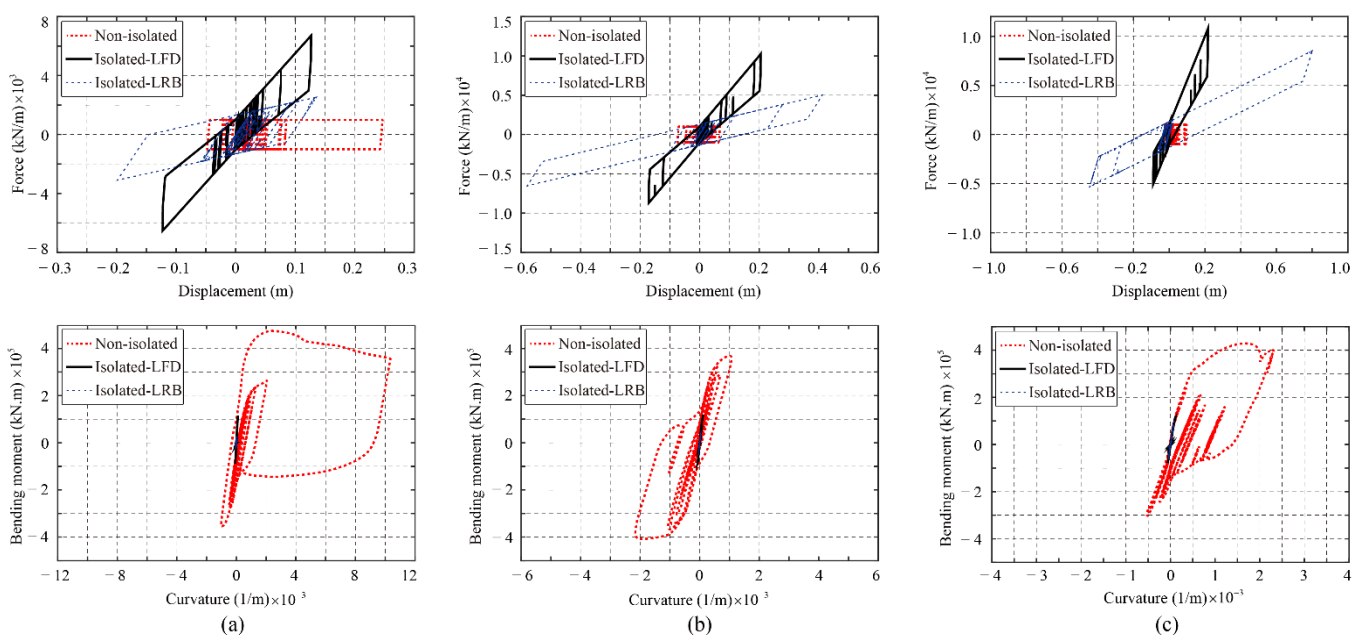


**Figure 11.** Force–displacement relationship of the continuous girder bridge for the original system (Non-isolated), LFD system (Isolated-LFD), and LRB system (Isolated-LRB) with (a) wave 4, (b) wave 9, and (c) wave 14 in Table 1.

It also can be seen from Figure 11 that the pier force–displacement relationships of the original system (Non-isolated) and isolation system (Isolated-LFD, Isolated-LRB) are significantly different. The pier with the fixed bearing experiences a huge hysteretic loop, which severely damages the pier. The piers maintain elasticity for the isolation systems (Isolated-LFD, Isolated-LRB). The seismic responses of the piers for the isolation systems are much smaller than that for the non-isolated system. Therefore, the substructure of the isolation systems (Isolated-LFD, Isolated-LRB) can effectively be protected from damage. This benefit can be explained below: For the original system (Non-isolated), the superstructure and the substructure are rigidly connected by the fixed bearing, and the

inertial force of the superstructure is mainly transmitted by the fixed bearing. However, for the isolation system (Isolated-LFD, Isolated-LRB), the inertial force of the superstructure is mainly transmitted both from piers 3 and 4. Conversely, the effects of velocity pulses are mitigated by the large relative displacement between the superstructure and substructure provided by the isolation system.

### 5.3. Bearing Displacement in the Longitudinal Direction

Figure 12 presents the bearing displacement time histories at pier 4 for the original system (Non-isolated), LFD system (Isolated-LFD), and LRB system (Isolated-LRB). It can be observed that large displacement pulses occur for all systems. This is because the large displacement caused by ground motions with velocity pulses must be undertaken either by the superstructure or the substructure. For the original system (Non-isolated), this displacement is taken by the pier with a fixed bearing. In contrast, for the isolation system (Isolated-LFD, Isolated-LRB), this displacement is accommodated by LFD and LRB. The relative displacement between the superstructure and the substructure of the LRB system (Isolated-LRB) is usually larger than that of the LFD system (Isolated-LFD). Moreover, the explanation of this phenomenon can be found in Section 5.2. Figure 13 shows the maximum bearing displacement at pier 4 for the original system (Non-isolated), LFD system (Isolated-LFD), and LRB system (Isolated-LRB) with 16 ground motions in Table 1. For the LRB system (Isolated-LRB), the large relative displacement between the superstructure and the substructure frequently occurs, and this large displacement far exceeds the allowable displacement of LRB (0.3 m). As a result, pounding and unseating of the superstructure of the bridge will happen under ground motion with strong velocity pulses. Meanwhile, LRBs are expected to experience severe damage. However, the maximum bearing displacements for the LFD system (Isolated-LFD) can be effectively controlled.

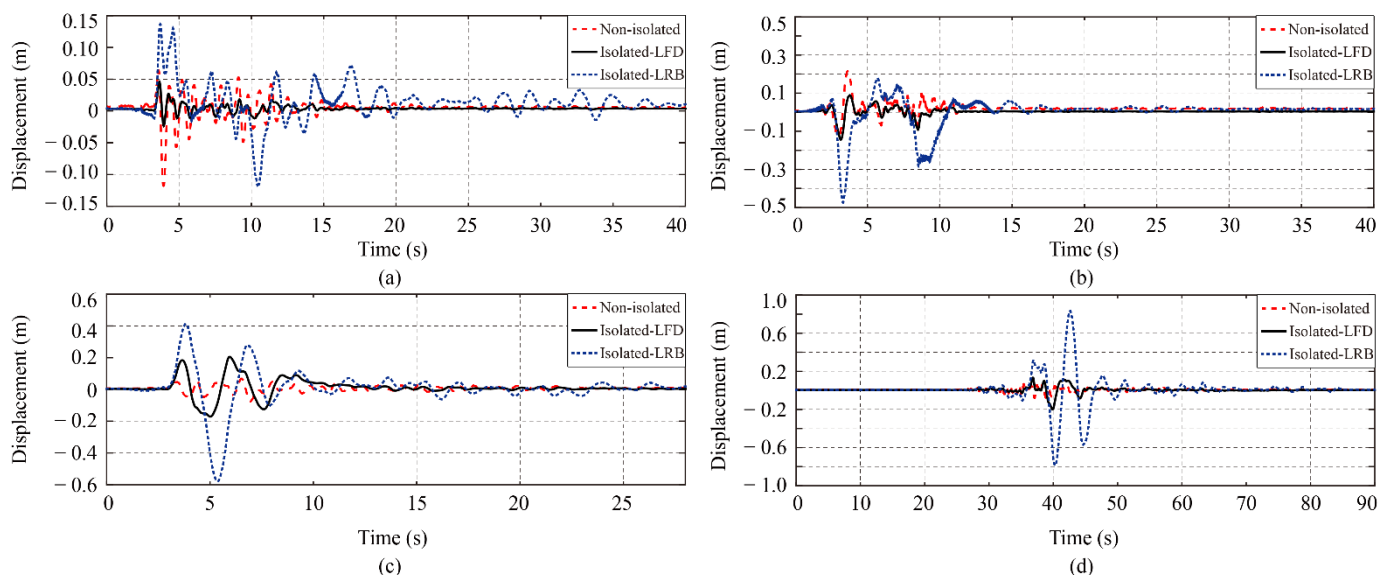


**Figure 12.** Relative displacement within the bearing time histories at pier 4 for the original system (Non-isolated), LFD system (Isolated-LFD), and LRB system (Isolated-LRB) with (a) wave 2, (b) wave 6, (c) wave 9, and (d) wave 12 in Table 1.

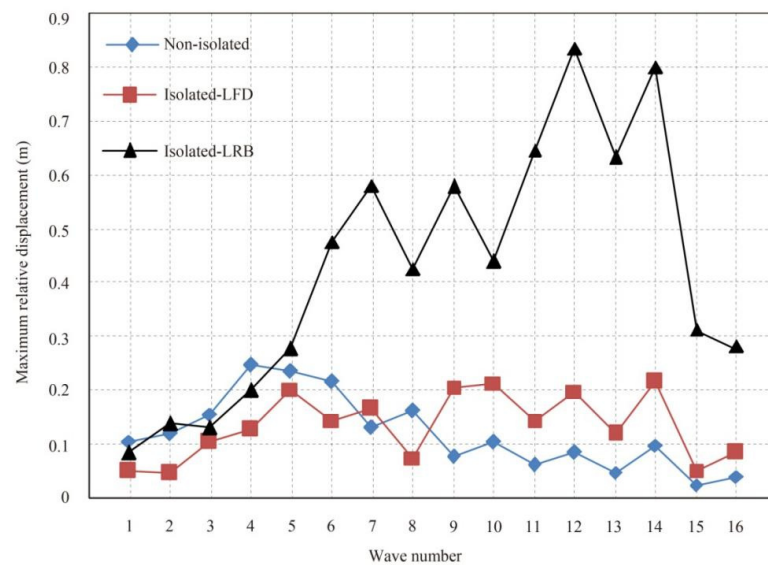


**Figure 13.** Maximum bearing displacement at pier 4 for the original system (Non-isolated), LFD system (Isolated-LFD), and LRB system (Isolated-LRB) with ground motions in Table 1.

#### 5.4. Pier Curvature in the Longitudinal Direction

Piers are expected to enter strong nonlinearity for ground motions with velocity pulses. Thus, curvature is adopted to evaluate the seismic responses of piers. The ratios of maximum pier curvature to its yielding curvature for ground motions in Table 1 are presented in Table 2. It shows that the maximum curvatures of pier 3 for the isolation systems are much smaller than those for the original system. Moreover, most of the maximum curvature in pier 3 for the isolation systems decreases by 90%. The first yield curvature of the section at the bottom of pier 3 is 0.00082 1/m, and the maximum pier curvatures for the isolation systems are smaller than the first yield curvature of the pier section. The maximum curvature in pier 4 for the original system (Non-isolated) is relatively small because the sliding bearing is applied at the top of pier 4. Thus, pier 4 is isolated from the superstructure, and only friction force can be transmitted. Based on the aforementioned discussion, it can be concluded that the proposed device (LFD) can effectively reduce the seismic responses of the substructure due to its capability of accommodating large relative displacement induced by velocity pulses. For structures subjected to ground motions with velocity pulses, accommodating large displacement is more important than dissipating energy.

**Table 2.** The ratios of maximum pier curvature to yielding curvature for the three systems.

Earthquake Number	Pier 3			Pier 4		
	Non-Isolated	Isolated-LRB	Isolated-LFD	Non-Isolated	Isolated-LRB	Isolated-LFD
1	0.09	0.03	0.10	0.07	0.03	0.09
2	<b>5.67</b>	0.02	0.57	0.07	0.02	0.55
3	<b>6.99</b>	0.03	0.11	0.07	0.03	0.11
4	<b>12.62</b>	0.03	0.14	0.07	0.03	0.15
5	<b>11.11</b>	0.03	0.93	0.07	0.03	0.76
6	<b>11.36</b>	0.07	0.42	0.07	0.07	0.43
7	<b>4.10</b>	0.05	0.28	0.07	0.06	0.28
8	<b>7.72</b>	0.05	0.68	0.07	0.06	0.69
9	<b>2.64</b>	0.05	0.14	0.07	0.05	0.16
10	<b>3.95</b>	0.06	0.16	0.07	0.06	0.18
11	<b>1.24</b>	0.06	0.10	0.07	0.06	0.08
12	<b>2.91</b>	0.07	0.10	0.07	0.08	0.10
13	<b>1.29</b>	0.05	0.10	0.07	0.06	0.08
14	<b>2.82</b>	0.10	0.14	0.07	0.10	0.16
15	0.22	0.03	0.10	0.07	0.03	0.08
16	0.88	0.03	0.10	0.07	0.03	0.08

## 6. Conclusions

The current research investigates the effects of the proposed linear friction damper (LFD) on the seismic responses of a continuous girder bridge subjected to ground motions with velocity pulses. First, the working mechanism and the force–displacement relationship of LFD are described in detail. Then, a numerical experiment is designed to validate the proposed constitutive model of LFD. In addition, the design process of LFD for a specific case is also illustrated. Second, three-span continuous girder bridges for the original system (Non-isolated), LFD system (Isolated-LFD), and LRB system (Isolated-LRB) are established by OpenSees. Third, 16 ground motions with velocity pulses are selected from the PEER ground motion database. Daubechies wavelet of order 4 is adopted to extract the maximum velocity pulse from the two orthogonal components of a ground motion. Then, the effects of the initial gap, the coefficient of friction, and the spring stiffness of LFD on the seismic responses of the bridge are analyzed. Finally, the seismic responses in the longitudinal direction of the bridge, including the force–displacement relationship, relative displacement within the bearing, and curvature at the bottom of the pier, are calculated and intensively discussed. Based on the numerical results, the main conclusions are summarized below:

The bearings of the LRB system usually experience large relative displacement due to its small post-yielding stiffness for ground motions with strong velocity pulses. Piers with fixed bearings are severely damaged, and this disadvantage is eliminated for the isolation systems (Isolated-LFD, Isolated-LRB). This phenomenon can be explained because for the original system (Non-isolated), the superstructure and substructure are rigidly connected by the fixed bearing. The inertial force is mainly transmitted through the pier with a fixed bearing. However, for the isolation systems (Isolated-LFD, Isolated-LRB), the velocity pulses are accommodated. Thus, piers are isolated from the inertial force of the superstructure.

According to the bearing displacement analysis, the relative displacement within the bearing can be effectively controlled for the LFD system (Isolated-LFD). Thus, pounding and unseating of the superstructure can be mitigated. The LFD system (Isolated-LFD) can balance between controlling the maximum bearing displacement and mitigating the damages of the pier compared with the other two systems (Non-isolated, Isolated-LRB).

The current research focuses on the basic concept of LFD, and the Coulomb friction law is adopted in the numerical experiment. In future research, a friction coefficient depending on the sliding velocity and contact pressure will be used in the constitutive model of LFD. In addition, more accurate hysteresis models available in the literature [29,30] will be adopted to improve the accuracy of the results.

**Author Contributions:** Conceptualization, H.L., C.Z., S.C. and X.D.; methodology, C.Z.; investigation, H.L.; writing—original draft preparation, J.G.; writing—review and editing, S.C.; supervision, X.D.; formal analysis, J.G.; validation, X.D. All authors have read and agreed to the published version of the manuscript.

**Funding:** This research was funded by the National Key Research and Development Program of China (2019YFE0112300); the National Natural Science Foundation of China (51978512); The Shanghai Post-doctoral Excellent Program (2021333); The Post-doctoral Innovation Practice Base Program of Shanghai Yangpu District; and the Transportation science and technology plan of Shandong province (2017B75).

**Institutional Review Board Statement:** Not applicable.

**Informed Consent Statement:** Not applicable.

**Data Availability Statement:** Not applicable.

**Conflicts of Interest:** The authors declare no conflict of interest.

## References

1. Yen, W.P.; Chen, G.; Yashinski, M.; Hashash, Y.; Holub, C.; Wang, K.; Guo, X. Lessons in bridge damage learned from the Wenchuan earthquake. *Earthq. Eng. Eng. Vib.* **2009**, *8*, 275–285. [[CrossRef](#)]
2. Kawashima, K.; Takahashi, Y.; Ge, H.; Wu, Z.; Zhang, J. Reconnaissance report on damage of bridges in 2008 Wenchuan, China, earthquake. *J. Earthq. Eng.* **2009**, *13*, 965–996. [[CrossRef](#)]
3. Sun, Z.; Wang, D.; Guo, X.; Si, B.; Huo, Y. Lessons learned from the damaged Huilan interchange in the 2008 Wenchuan earthquake. *J. Bridge Eng.* **2011**, *17*, 15–24. [[CrossRef](#)]
4. Sehhati, R.; Rodriguez-Marek, A.; ElGawady, M.; Cofer, W.F. Effects of near-fault ground motions and equivalent pulses on multi-story structures. *Eng. Struct.* **2011**, *33*, 767–779. [[CrossRef](#)]
5. Ismail, M.; Casas, J.R.; Rodellar, J. Near-fault isolation of cable-stayed bridges using RNC isolator. *Eng. Struct.* **2013**, *56*, 327–342. [[CrossRef](#)]
6. Ates, S.; Constantinou, M.C. Example of application of response spectrum analysis for seismically isolated curved bridges including soil-foundation effects. *Soil Dyn. Earthq. Eng.* **2011**, *31*, 648–661. [[CrossRef](#)]
7. Bhuiyan, A.R.; Alam, M.S. Seismic performance assessment of highway bridges equipped with superelastic shape memory alloy-based laminated rubber isolation bearing. *Eng. Struct.* **2013**, *49*, 396–407. [[CrossRef](#)]
8. Galindo, C.M.; Belda, J.G.; Hayashikawa, T. Non-linear seismic dynamic response of curved steel bridges equipped with LRB supports. *Steel Constr.* **2010**, *3*, 34–41. [[CrossRef](#)]
9. Monzon, E.V.; Buckle, I.G.; Itani, A.M. Seismic Performance and Response of Seismically Isolated Curved Steel I-Girder Bridge. *J. Struct. Eng.* **2016**, *142*, 04016121. [[CrossRef](#)]
10. Tanaka, R.; Galindo, C.M.; Hayashikawa, T. Nonlinear seismic dynamic response of continuous curved highway viaducts with different bearing supports. *World Acad. Sci. Eng. Technol.* **2009**, *5*, 327–333.
11. Losanno, D.; Palumbo, F.; Calabrese, A.; Barrasso, T.; Vaiana, N. Preliminary investigation of aging effects on recycled rubber fiber reinforced bearings (RR-FRBs). *J. Earthq. Eng.* **2021**, 1–18. [[CrossRef](#)]
12. Kataria, N.P.; Jangid, R.S. Seismic protection of the horizontally curved bridge with semi-active variable stiffness damper and isolation system. *Adv. Struct. Eng.* **2016**, *19*, 1103–1117. [[CrossRef](#)]
13. Dicleli, M.; Milani, A.S. *Steel Hysteretic Damper Featuring Displacement Dependent Hardening for Seismic Protection of Structures*; Springer: New Delhi, India, 2015.
14. Chen, Z.Y.; Chen, W.; Bian, G.Q. Seismic Performance Upgrading for Underground Structures by Introducing Shear Panel Dampers. *Adv. Struct. Eng.* **2014**, *17*, 1343–1358. [[CrossRef](#)]
15. Providakis, C.P. Effect of LRB isolators and supplemental viscous dampers on seismic isolated buildings under near-fault excitations. *Eng. Struct.* **2008**, *30*, 1187–1198. [[CrossRef](#)]
16. Liao, W.-I.; Loh, C.-H.; Lee, B.-H. Comparison of dynamic response of isolated and non-isolated continuous girder bridges subjected to near-fault ground motions. *Eng. Struct.* **2004**, *26*, 2173–2183. [[CrossRef](#)]
17. Panchal, V.R.; Jangid, R.S. Variable friction pendulum system for near-fault ground motions. *Struct. Control Health Monit.* **2008**, *15*, 568–584. [[CrossRef](#)]
18. Karalar, M.; Padgett, J.E.; Dicleli, M. Parametric analysis of optimum isolator properties for bridges susceptible to near-fault ground motions. *Eng. Struct.* **2012**, *40*, 276–287. [[CrossRef](#)]
19. Li, S.; Dezfuli, F.H.; Wang, J.-Q.; Alam, M.S. Longitudinal seismic response control of long-span cable-stayed bridges using shape memory alloy wire-based lead rubber bearings under near-fault records. *J. Intell. Mater. Syst. Struct.* **2017**, *29*, 703–728. [[CrossRef](#)]
20. Dolce, M.; Cardone, D.; Croatto, F. Frictional Behavior of Steel-PTFE Interfaces for Seismic Isolation. *Bull. Earthq. Eng.* **2005**, *3*, 75–99. [[CrossRef](#)]
21. Alam, M.S.; Bhuiyan, M.A.R.; Billah, A.H.M.M. Erratum to: Seismic fragility assessment of SMA-bar restrained multi-span continuous highway bridge isolated by different laminated rubber bearings in medium to strong seismic risk zones. *Bull. Earthq. Eng.* **2012**, *10*, 1911–1913. [[CrossRef](#)]
22. Mckenna, F.; Scott, M.H.; Fennes, G.L. Nonlinear Finite-Element Analysis Software Architecture Using Object Composition. *J. Comput. Civ. Eng.* **2010**, *24*, 95–107. [[CrossRef](#)]
23. Mander, J.B.; Priestley, M.J.N.; Park, R. Theoretical Stress-Strain Model for Confined Concrete. *J. Struct. Eng.* **1988**, *114*, 1804–1826. [[CrossRef](#)]
24. Shahi, S.K.; Baker, J.W. An Efficient Algorithm to Identify Strong-Velocity Pulses in Multicomponent Ground Motions. *Bull. Seismol. Soc. Am.* **2014**, *104*, 2456–2466. [[CrossRef](#)]
25. Baker, J.W. Quantitative Classification of Near-Fault Ground Motions Using Wavelet Analysis. *Bull. Seismol. Soc. Am.* **2007**, *97*, 1486–1501. [[CrossRef](#)]
26. Box, G.E.P.; Wilson, K.B. *On the Experimental Attainment of Optimum Conditions*; Springer: New York, NY, USA, 1992; pp. 270–310.
27. Guo, J.J.; Zhong, J.; Dang, X.Z.; Yuan, W.C. Seismic performance assessment of a curved bridge equipped with a new type spring restrainer. *Eng. Struct.* **2017**, *151*, 105–114. [[CrossRef](#)]
28. Towashiraporn, P. Building seismic fragilities using response surface metamodells. *Ga. Inst. Technol.* **2004**, *104*, 2456–2466.

29. Vaiana, N.; Sessa, S.; Marmo, F.; Rosati, L. A class of uniaxial phenomenological models for simulating hysteretic phenomena in rate-independent mechanical systems and materials. *Nonlinear Dyn.* **2018**, *93*, 1647–1669. [[CrossRef](#)]
30. Vaiana, N.; Sessa, S.; Rosati, L. A generalized class of uniaxial rate-independent models for simulating asymmetric mechanical hysteresis phenomena. *Mech. Syst. Signal Process.* **2021**, *146*, 106984. [[CrossRef](#)]